# Assessment of the Multi-Beam Performance of Wideband Arrays Using the Observable Field

Ozzola, Riccardo; Tadolini, Cesare; Tapia Barroso, Roderick G.; Imberg, Ulrik; Freni, A.; Cavallo, Daniele; Neto, Andrea

**DOI**
10.1109/TAP.2025.3599268



**Publication date**
2025

**Document Version**
Final published version

**Published in**
IEEE Transactions on Antennas and Propagation

# Communication

## Assessment of the Multibeam Performance of Wideband Arrays Using the Observable Field

Riccardo Ozzola, Cesare Tadolini, Roderick G. Tapia Barroso, Ulrik Imberg, Angelo Freni, Daniele Cavallo, and Andrea Neto

***Abstract*—Multibeam systems are a key technology for the high-speed links of the next-generation communication standards. Due to the stringent space constraints for allocating antennas on a platform, it is of paramount importance to assess—with respect to the physical size—the multibeam performance of the antenna in terms of the maximum number of simultaneous orthogonal beams. This is done by resorting to the concept of the observable field, which is here extended to planar domains. Then, this concept is used to assess the multibeam performance of a wideband phased array prototype developed for mobile communications. The signal-to-interference ratio (SIR), computed from the measured radiation patterns of the prototype, is analyzed versus the frequency and the number of beams and compared to the benchmark case of an ideal antenna radiating the observable field.**

***Index Terms*—Fundamental bounds, multibeam, observable field, phased array.**

### I. Introduction

The next-generation communication standards can reach high data rates employing massive multiple-input–multiple-output (MIMO) or multibeam systems [1], [2]. Specifically, antennas will be required to radiate directive beams toward the different users, distributed over a wide field of view (FoV). Moreover, several bands are already in use in both the microwave and the millimeter-wave bands [3]. The state-of-the-art base stations employ resonant radiators, which, due to their narrowband properties, require several antennas to operate over multiple bands, therefore increasing the complexity and the overall allocated space. For these reasons, wideband and wide-angle scanning array solutions have received attention for mobile communications [4], [5], [6], [7], [8].

Wideband phased arrays can operate in an MIMO configuration despite the high interelement mutual coupling, as recently discussed in [9], [10], [11], and [12]. In particular, in [10], it was dispelled the misconception that the mutual coupling between the feeding ports necessarily hinders the MIMO properties. There, it was shown that, for coherently excited arrays, orthogonal radiation patterns can be obtained regardless of the interelement mutual coupling and that the orthogonality levels depend only on the beam overlap, the beamwidth, and the sidelobes. The connected arrays [13] are good candidates for realizing such wideband and wide-angle scanning antennas. This concept is compatible with a planar implementation based on multilayer printed circuit boards (PCBs) [14]. The telecommunication community has recently recognized the potential of wideband connected arrays to enhance the channel capacity in MIMO systems [11].

In [8], an $8 \times 8$ prototype of a dual-polarized connected slot array with a 4:1 bandwidth was designed and measured. As the prototype is not electrically large, with a side of approximately four wavelengths at the maximum frequency, the assessment of the number of orthogonal beams of the array is not straightforward. The traditional approach is based on the concept of the degrees of freedom [15] and the fundamental bounds of the radiating structures [16], [17]. The problem of quantifying the MIMO bounds of antennas has been the topic of several recent publications [18], [19], [20], [21], [22], [23], [24], [25], [26], [27]. However, these works mainly address resonant antennas, large platforms, or idealized geometries, whereas, in [28], a more general study is carried out by means of a singular value decomposition of the scattering matrix associated with the multiport antenna.

In this communication, the observable field, introduced in [29] and [30] for spherical domains, is extended to the study of planar domains and used to assess the multibeam performance of wideband arrays. More specifically, measured radiation patterns from a connected array prototype are used to compute the signal-to-interference ratio (SIR) when multiple beams are generated. Maps of the SIR as a function of the frequency and the number of beams are presented and compared to an ideal radiating aperture with the same size as the array.

### II. Observable Field From Planar Domains

#### A. General Definition

The observable field $\mathbf{E}^{\text{obs}}$ is the component of the incident electromagnetic field $(\mathbf{E}^i, \mathbf{H}^i)$ that can interact with a finite-size antenna, as discussed in [29] and [30]. We refer to the antenna bounding surface as $\mathcal{S}$, and we assume that it is surrounded by free space, as shown in Fig. 1. The observable field can be expressed as the superposition of an inward and an outward propagating wave

$$\mathbf{E}^{\text{obs}}(\mathbf{r}) = \mathbf{E}^{\text{obs}}_{\text{inw}}(\mathbf{r}) + \mathbf{E}^{\text{obs}}_{\text{out}}(\mathbf{r}) \tag{1}$$

which are defined in the antenna far field as the following product:

$$\mathbf{E}^{\text{obs}}_{\text{inw/out}}(\mathbf{r}) = \mathbf{V}^{\text{obs}}_{\text{inw/out}}\left(\hat{\mathbf{k}}\right) \frac{e^{\pm jk_0 r}}{r} \tag{2}$$

where $\mathbf{V}^{\text{obs}}_{\text{inw/out}}$ is the far-field pattern of either the inward or outward component, having $\hat{\mathbf{k}} = \sin\theta\cos\phi\hat{\mathbf{x}} + \sin\theta\sin\phi\hat{\mathbf{y}} + \cos\theta\hat{\mathbf{z}}$ as the angular variable. The upper and lower signs "$\pm$" in the phase term refer to the inward and outward components, respectively. The ideal antenna bounded by $\mathcal{S}$, which radiates the outward component of the observable field, is the maximum-gain antenna within the assigned physical boundaries.

In [29] and [30], the observable field is calculated as the radiation from currents that are proportional to the equivalent currents defined

Received 13 February 2025; revised 4 July 2025; accepted 3 August 2025. Date of publication 21 August 2025; date of current version 18 December 2025. This work was supported by HUAWEI Technologies Sweden AB, UNB Project, under Grant YBN2020045031. *(Corresponding author: Riccardo Ozzola.)*

Riccardo Ozzola, Cesare Tadolini, Roderick G. Tapia Barroso, Daniele Cavallo, and Andrea Neto are with the Microelectronics Department, Faculty of Electrical Engineering, Mathematics and Computer Science, Delft University of Technology, 2628 CD Delft, The Netherlands (e-mail: R.Ozzola-1@tudelft.nl).

Ulrik Imberg is with Huawei Technologies Sweden AB, 164 40 Kista, Sweden.

Angelo Freni is with the Department of Information Engineering, University of Florence, 50139 Florence, Italy.

Digital Object Identifier 10.1109/TAP.2025.3599268

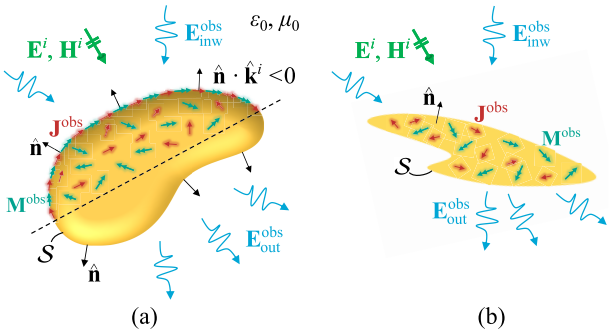


Fig. 1. (a) Sketch of the incident field $(\mathbf{E}^i, \mathbf{H}^i)$ impinging into the domain bounded by $\mathcal{S}$. From the illuminated portion of $\mathcal{S}$, the currents radiate the inward and outward components of the observable field and (b) its extension to the planar case.

on the surface $\mathcal{S}$ and truncated according to the physical optics approximation. The currents that radiate the outward propagating waves are defined as follows:

$$\mathbf{J}_{\text{out}} = \begin{cases} -\hat{\mathbf{n}} \times \mathbf{H}^i, & \text{if } \hat{\mathbf{n}} \cdot \hat{\mathbf{k}}^i < 0 \\ 0, & \text{otherwise} \end{cases} \tag{3}$$

$$\mathbf{M}_{\text{out}} = \begin{cases} \hat{\mathbf{n}} \times \mathbf{E}^i, & \text{if } \hat{\mathbf{n}} \cdot \hat{\mathbf{k}}^i < 0 \\ 0, & \text{otherwise} \end{cases} \tag{4}$$

where $\hat{\mathbf{n}}$ is the outwardly oriented normal unit vector of $\mathcal{S}$ and $\hat{\mathbf{k}}^i$ is the plane-wave direction of the incidence. A more generic incident field can also be considered by expanding it in a plane-wave spectrum [30]. The inwardly propagating fields are sustained by the currents $\mathbf{J}_{\text{inw}}$ and $\mathbf{M}_{\text{inw}}$, which are related to $\mathbf{J}_{\text{out}}$ and $\mathbf{M}_{\text{out}}$ as follows:

$$\begin{pmatrix} \mathbf{J}_{\text{inw}} \\ \mathbf{M}_{\text{inw}} \end{pmatrix} = \begin{pmatrix} -\mathbf{J}_{\text{out}} \\ \mathbf{M}_{\text{out}} \end{pmatrix}^* \tag{5}$$

where symbol "*" represents the complex conjugate.

The currents $\mathbf{J}^{\text{obs}}_{\text{inw/out}}$ and $\mathbf{M}^{\text{obs}}_{\text{inw/out}}$ that radiate the observable field are obtained with the following proportionality relation:

$$\begin{pmatrix} \mathbf{J}^{\text{obs}}_{\text{inw/out}} \\ \mathbf{M}^{\text{obs}}_{\text{inw/out}} \end{pmatrix} = \alpha \begin{pmatrix} \mathbf{J}_{\text{inw/out}} \\ \mathbf{M}_{\text{inw/out}} \end{pmatrix} \tag{6}$$

where $\alpha$ is a scaling factor, which enforces that the effective area of the antenna tends to a nonzero value also for vanishing physical areas. The values of $\alpha$ can, in general, be calculated with the procedure in [30, eq.(9)]. However, for the single plane-wave incidence case, this simplifies to [29 eq.(31)] as the ratio between the effective and the physical area.

The observable field pattern is evaluated as the integral

$$\mathbf{V}^{\text{obs}}_{\text{inw/out}}\left(\hat{\mathbf{k}}\right) = \left[ -j\omega \frac{\mu_0}{4\pi} (\bar{\bar{\mathbf{I}}} - \hat{\mathbf{r}}\hat{\mathbf{r}}) \cdot \iint_{\mathcal{S}} \mathbf{J}^{\text{obs}}_{\text{inw/out}}(\mathbf{r}') e^{jk_0 \hat{\mathbf{k}} \cdot \mathbf{r}'} d\mathbf{r}' + jk_0 \hat{\mathbf{r}} \times \iint_{\mathcal{S}} \mathbf{M}^{\text{obs}}_{\text{inw/out}}(\mathbf{r}') e^{jk_0 \hat{\mathbf{k}} \cdot \mathbf{r}'} d\mathbf{r}' \right]. \tag{7}$$

The integrals in (7) allow us to calculate the observable field associated with any antenna geometry. In [29], it is shown that, for a single plane wave impinging on a sphere, the observable field is the Airy pattern of the disk orthogonal to the direction of incidence. For the case of spherical volumes, due to the rotational symmetry of the geometry, the patterns are shape-invariant with respect to the angle of incidence. However, this is not valid for arbitrary shapes, where the radiating surface has to be projected toward the direction of observation, giving rise to the scan loss effect. In this regard, this is in line with the considerations of [27], where the cross section, or the more general concept of the average shadow area, is linked to the degrees of freedom of the electromagnetic fields.

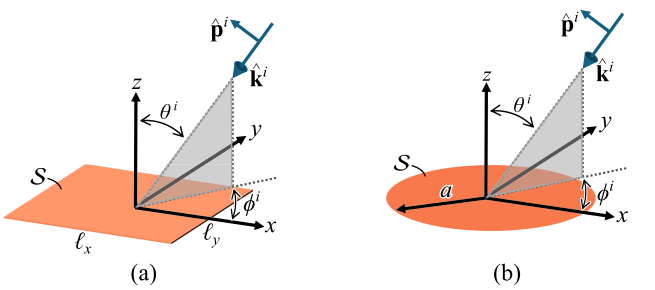


Fig. 2. Sketch of a plane-wave impinging into (a) rectangle and (b) circle.

This formulation can be extended to the case when $\mathcal{S}$ is a planar surface and no inner region is defined. This does not cause any loss of generality as no field sources are located in the volume bounded by $\mathcal{S}$ and the currents $\mathbf{J}^{\text{obs}}_{\text{inw/out}}$ and $\mathbf{M}^{\text{obs}}_{\text{inw/out}}$ are located on the surface. The normal unit vector $\hat{\mathbf{n}}$ is chosen such that $\hat{\mathbf{n}} \cdot \hat{\mathbf{k}}^i < 0$. With such a choice, the outward and the inward observable field are diverging from and converging to the structure, respectively, as shown in Fig. 1(b).

### B. Observable Field From Rectangular and Circular Surfaces

For practical applications, it is worth investigating the observable field from planar domains under a plane-wave illumination. In particular, for specific shapes of $\mathcal{S}$, the integrals of (7) can be solved analytically, as described in [31].

Let us consider a plane wave with direction of incidence $\hat{\mathbf{k}}^i$, corresponding to the angles $(\theta^i, \phi^i)$, and its electric field has amplitude $|E_0|$ and is oriented along $\hat{\mathbf{p}}^i$. Therefore, the incident field can be written as follows:

$$\mathbf{E}^i(\mathbf{r}) = |E_0| e^{-jk_0 \hat{\mathbf{k}}^i \cdot \mathbf{r}} \hat{\mathbf{p}}^i. \tag{8}$$

We assume that $\mathcal{S}$ is a rectangle placed in the $xy$ plane, with sides of length $\ell_x$ and $\ell_y$ and parallel to the axes $x$ and $y$, respectively [see Fig. 2(a)]. As the normal unit vector is constant over $\mathcal{S}$ and equal to $\hat{\mathbf{z}}$, by using the plane-wave relation between electric and magnetic field to calculate the currents, and thanks to the properties of the Fourier transform, the outward observable pattern in (7) simplifies to

$$\mathbf{V}^{\text{obs}}_{\text{out}}\left(\hat{\mathbf{k}}\right) = j \frac{k_0 \alpha |E_0| \ell_x \ell_y}{4\pi} \operatorname{sinc}\left(\ell_x \frac{k_x - k_x^i}{2}\right) \operatorname{sinc}\left(\ell_y \frac{k_y - k_y^i}{2}\right) \mathbf{p}^{\text{obs}} \tag{9}$$

where $\operatorname{sinc}(x) = \sin(x)/x$ and

$$\mathbf{p}^{\text{obs}} = (\bar{\bar{\mathbf{I}}} - \hat{\mathbf{r}}\hat{\mathbf{r}}) \cdot \left[\hat{\mathbf{z}} \times (\hat{\mathbf{k}}^i \times \hat{\mathbf{p}}^i)\right] - \hat{\mathbf{r}} \times (\hat{\mathbf{z}} \times \hat{\mathbf{p}}^i) \tag{10}$$

with $k_x^i = k_0 \hat{\mathbf{k}}^i \cdot \hat{\mathbf{x}}$ and $k_y^i = k_0 \hat{\mathbf{k}}^i \cdot \hat{\mathbf{y}}$.

To assess the performance of planar circular antennas such as [32], [33], [34], it is meaningful to calculate the observable field for a circle of radius $a$ located in the $xy$ plane, as sketched in Fig. 2(b). The outward observable pattern can be evaluated as

$$\mathbf{V}^{\text{obs}}_{\text{out}}\left(\hat{\mathbf{k}}\right) = j \frac{\alpha a |E_0|}{2} \frac{F\left(\hat{\mathbf{k}}\right)}{\sin^2 \theta^i - \sin^2 \theta} \mathbf{p}^{\text{obs}} \tag{11}$$

where

$$F\left(\hat{\mathbf{k}}\right) = \chi_1(\theta) + 2 \sum_{n=1}^{\infty} \cos(n(\phi - \phi^i)) \chi_2(\theta, n) \tag{12}$$

and

$$\chi_1(\theta) = \sin\theta^i J_1(k_0 a \sin\theta^i) J_0(k_0 a \sin\theta) - \sin\theta J_0(k_0 a \sin\theta^i) J_1(k_0 a \sin\theta) \tag{13}$$

$$\chi_2(\theta, n) = \sin\theta J_n(k_0 a \sin\theta^i) J_{n-1}(k_0 a \sin\theta) - \sin\theta^i J_{n-1}(k_0 a \sin\theta^i) J_n(k_0 a \sin\theta). \tag{14}$$

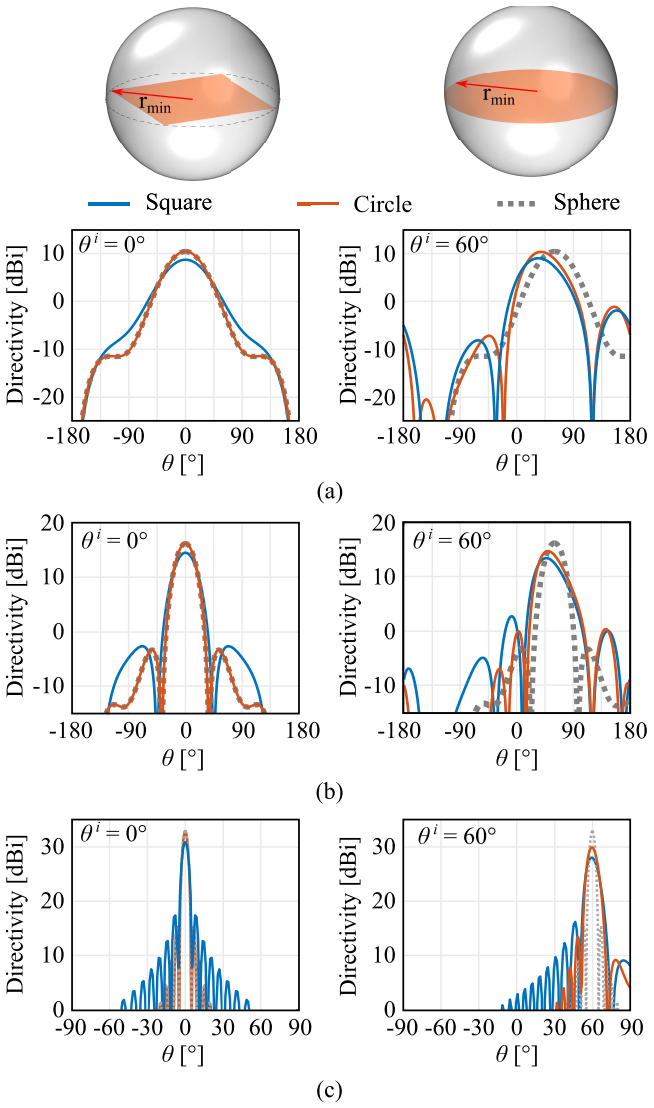


Fig. 3. Comparison of the observable field patterns for a square, a circle, and their enclosing sphere of radius (a) $r_{\min} = 0.5\lambda_0$, (b) $r_{\min} = \lambda_0$, and (c) $r_{\min} = 7\lambda_0$, for a plane wave impinging from $\theta^i = 0°$ (left) and $\theta^i = 60°$ (right) on the plane $\phi^i = 0°$.

$J_n$ in (13) and (14) is the $n$th order Bessel function of the first kind. In the numerical implementation, the infinite sum of (12) is truncated to the least integer greater than or equal to $k_0 a$.

Finally, the inward component of the observable pattern can be calculated from the outward component in (9) and (11) by applying the transformation

$$\begin{pmatrix} \mathbf{V}^{\text{obs}}_{\text{inw}}\left(\hat{\mathbf{k}}\right)\cdot\hat{\boldsymbol{\theta}} \\ \mathbf{V}^{\text{obs}}_{\text{inw}}\left(\hat{\mathbf{k}}\right)\cdot\hat{\boldsymbol{\phi}} \end{pmatrix} = \begin{pmatrix} \mathbf{V}^{\text{obs}}_{\text{out}}\left(-\hat{\mathbf{k}}\right)\cdot\hat{\boldsymbol{\theta}} \\ -\mathbf{V}^{\text{obs}}_{\text{out}}\left(-\hat{\mathbf{k}}\right)\cdot\hat{\boldsymbol{\phi}} \end{pmatrix}. \tag{15}$$

In Fig. 3, the inward observable far-field patterns are compared for a square surface, a circular surface, and their enclosing sphere of radius $r_{\min}$. The plots have been obtained for a single plane wave impinging from $\phi^i = 0°$, and $\theta^i = 0°$ or $\theta^i = 60°$. For $\theta^i = 0°$, the patterns of the sphere and the circle are superimposed because the radiation from the sphere is equivalent to one from its cross section that coincides with the circle. Instead, in scanning conditions, e.g., for $\theta^i = 60°$ as in Fig. 3, the two patterns differ because the disk, unlike the sphere, is subject to the scan loss effect due to the decreasing projected area. For the planar cases, the scan loss tends to the $\cos\theta$ law for electrically large apertures, which is visible in Fig. 3(c). When

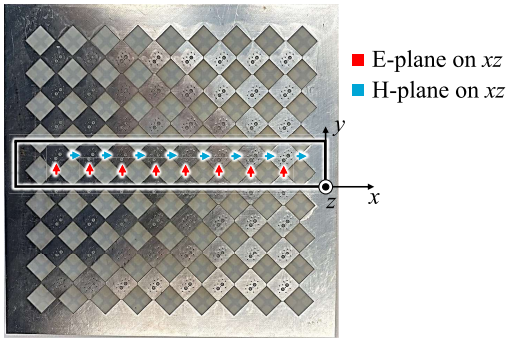


Fig. 4. Photograph of the 8 × 8 connected array [8], showing the elements for which the EEPs have been characterized.

scanning, the beam pointing angle for the smaller electrical sizes [see Fig. 3(a) and (b), right] is slightly closer to broadside than the nominal 60°. This is due to aberrations resulting from the dependence of $\mathbf{p}^{\text{obs}}$ on the angles $\theta$ and $\theta^i$ in (10). Such an effect is more evident for small electrical sizes, for which the main lobe is broad. The scan loss and the aberration are relevant in multibeam systems, as the antenna directivity reduces in the direction of interest and affects the link budget.

### C. Coupling Coefficients and SIR

Let us consider an antenna having a multibeam capability, whose pattern pointing toward the direction $\hat{\mathbf{k}}_n$ is referred to as $\mathbf{V}^{\text{a}}_n$. A wave impinges on the antenna from the direction $\hat{\mathbf{k}}_m$, and its associated observable field is referred to as $\mathbf{V}^{\text{obs}}_{\text{inw},m}$. The coupling between the observable field $\mathbf{V}^{\text{obs}}_{\text{inw},m}$ and the $n$th antenna beam $\mathbf{V}^{\text{a}}_n$ is defined as in [35]

$$C^{\text{obs,a}}_{mn} = \frac{\iint_{4\pi} \mathbf{V}^{\text{obs}}_{\text{inw},m}\left(\hat{\mathbf{k}}\right)\cdot\mathbf{V}^{\text{a}}_n\left(\hat{\mathbf{k}}\right)d\hat{\mathbf{k}}}{\sqrt{\iint_{4\pi}\left|\mathbf{V}^{\text{obs}}_{\text{inw},m}\left(\hat{\mathbf{k}}\right)\right|^2 d\hat{\mathbf{k}}\iint_{4\pi}\left|\mathbf{V}^{\text{a}}_n\left(\hat{\mathbf{k}}\right)\right|^2 d\hat{\mathbf{k}}}}. \tag{16}$$

The beam-coupling coefficients (16) are similar to the ones introduced by Stein [36]. However, these latter are calculated for the same transmitting antenna and are associated with the beam coupling and, consequently, port coupling.

In multibeam systems generated from arbitrary geometries, different values of $C^{\text{obs,a}}_{mn}$ arise for each pair of $m$ and $n$, and several terms have to be computed. The calculation of the integrals in (16) is efficiently computed with the Gauss–Legendre quadrature on the unitary sphere, as described in [37] and [38].

For $m = n$, the term $|C^{\text{obs,a}}_{mm}|^2$ can be interpreted as an antenna efficiency, which is equal to unity when the antenna pattern matches the observable field. It is worth noting that such efficiency is, unlike the aperture efficiency, always bounded by unity, regardless of the antenna size. The coupling coefficients $C^{\text{obs,a}}_{mn}$ can also be used to characterize the SIR of each beam. Assuming that $N_l$ uncorrelated links are present, the SIR for beam $m$, corresponding to the desired signal, is calculated as follows:

$$\text{SIR}_m = \frac{P^{\text{obs}}_m\left|C^{\text{obs,a}}_{mm}\right|^2}{\sum_{\substack{n=1\\n\neq m}}^{N_l} P^{\text{obs}}_n\left|C^{\text{obs,a}}_{mn}\right|^2} \tag{17}$$

where $P^{\text{obs}}_m$ and $P^{\text{obs}}_n$ are the observable power associated with the signal of beam $m$ and the interference $n \neq m$, respectively. The observable power is the power radiated by $\mathbf{J}_{\text{out}}$ and $\mathbf{M}_{\text{out}}$ and is computed as the integral over the full solid angle of the radiation intensity associated with the observable field.

## III. Performance Assessment of Multibeam Array

The theory of the observable field presented in Section II can be used to assess the multibeam performance of real antennas in terms

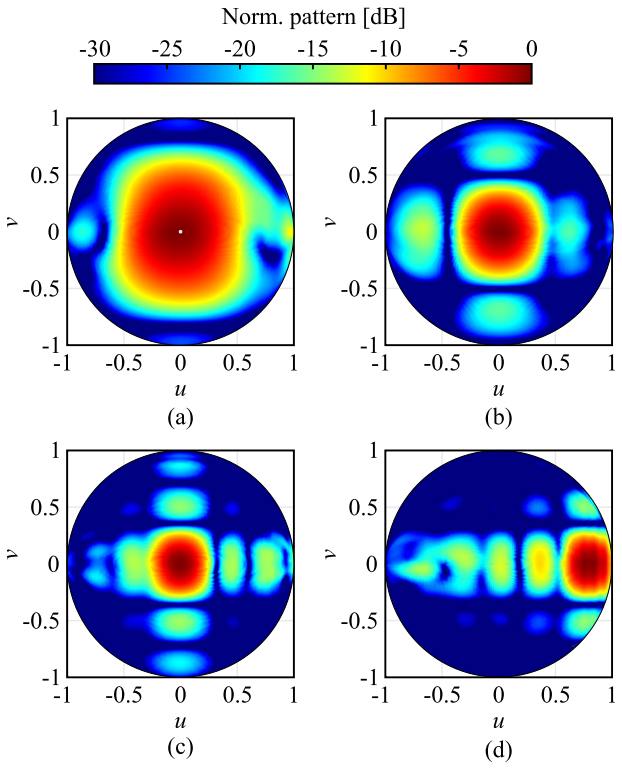


Fig. 5. Reconstruction of the array normalized patterns at (a) 3 GHz for broadside scanning, (b) 5 GHz for broadside scanning, (c) 7 GHz for broadside scanning, and (d) 7 GHz for scanning toward 60°.

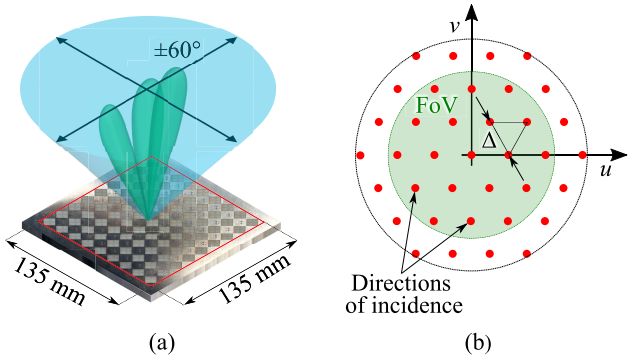


Fig. 6. (a) Sketch of the communication scenario where the antenna operates in the FoV ±60° with plane waves impinging from directions obtained from a sampling in the *uv* plane and (b) representation of the hexagonal sampling in the *uv* plane.

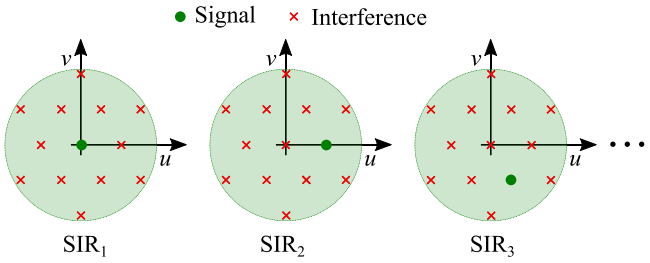


Fig. 7. Sketch of the calculation, for a certain number of beams, of the SIR for each beam.

of the SIR. To this purpose, the 8 × 8 dual-polarized connected slot array prototype of [8], shown in Fig. 4, is considered. The array used an artificial dielectric radome to operate in the frequency range from 2 to 8 GHz and to scan up to 60° in all the azimuthal planes. Only the embedded element patterns (EEPs) relevant to the elements belonging to the central row of the array, as highlighted in Fig. 4, were measured. These correspond to 16 EEPs characterized on the *xz* plane, which corresponds to eight EEPs in the E-plane for the *x*-polarized feeds and eight EEPs in the H-plane for the *y*-polarized feeds. All the other rows of the array are assumed to have the same patterns in the *xz* plane, while rotated patterns in the *yz* plane, interchanging the E- with H-plane. Finally, the EEPs in any other azimuth planes are reconstructed with the interpolation algorithm in [39]. The full array patterns are estimated with the coherent sum of the EEPs, including the complex weights for the different scanning conditions. Some examples of the reconstructed array patterns in the *uv* plane at different frequencies are given in Fig. 5 for different scanning conditions.

The observable field is used to assess the array performance in the scenario sketched in Fig. 6(a), where plane waves impinge into the antenna within a conical FoV of ±60°. As the antenna has been designed to operate and be matched in these scanning conditions. Plane waves impinging from outside this solid angle are not considered in the analysis. We assume that the directions of incidence are obtained from a uniform hexagonal sampling in the *uv* plane with sampling Δ, as shown in Fig. 6(b). Different configurations are investigated by reducing Δ. This operation reduces the angular separation between the impinging waves and increases the number of beams by multiples of six. Please note that a uniform sampling in the *uv* plane (as the one used in this communication) does not correspond to an equidistant sampling in the angular domain. For every configuration, all the possible coupling coefficients are calculated with (16). As sketched in Fig. 7, for each number of beams, all the SIRs are calculated, considering one of the beams as the signal and all other beams as interference. For each configuration, i.e., beam spacing-electrical area, the minimum SIR is calculated. The observable field used in the analysis pertains to the square plate containing the slots as shown in Fig. 6(a), i.e., $\ell_x = \ell_y = 135$ mm, and the patterns are calculated using (9).

In Fig. 8(a), the minimum SIR is calculated versus the electrical area, i.e., $\ell_x \times \ell_y/\lambda_0^2$, and the number of beams for the ideal antenna case, i.e., $\mathbf{V}^{\mathrm{a}} = \mathbf{V}^{\mathrm{obs}}$, which constitutes the benchmark, as the coupling with the impinging signal is maximized. A general upward trend in the number of usable beams (corresponding to smaller angular interbeam distance Δ) for a given SIR is observed when increasing the frequency, or equivalently, for larger electrical size. However, significant variations in SIR still occur due to the specific beam configuration. The white area is relevant to a SIR<0 dB and corresponds to a significant overlap between the main lobe of the ideal antenna pattern and the closest interferer. In Fig. 8(a), for the area bordered in red, the closest interferers are aligned with the first null of the desired beam pattern, as shown in the inset, exhibiting higher SIR levels. This is an optimal configuration where the SIR and the number of beams are jointly maximized. The green area corresponds to the configuration where the closest interferers are aligned with the second null of the pattern, as shown in the inset. This yields a higher rejection of the interference at the expense of a lower number of beams.

In Fig. 8(b), the SIR performance of the connected array prototype is studied. The coupling coefficients of (16) exploit the measured radiation patterns as $\mathbf{V}^{\mathrm{a}}$. The same trend as in Fig. 8(a) can be recognized, showing regions with higher SIR levels, where the interferers are aligned with the first and second nulls. However, the map exhibits a shift toward higher frequency and lower SIR values with respect to those in Fig. 8(a). In fact, the edge effects and the nonidealities of the physical antenna realization imply different array patterns from the observable field, which yields $|C^{mm}_{\mathrm{obs,a}}|^2 < 1$. These effects are summarized by the array efficiency in Fig. 9(a), calculated as $|C^{mm}_{\mathrm{obs,a}}|^2$ and averaged for each electrical area and beam configuration. An efficiency lower than one causes a shift of the

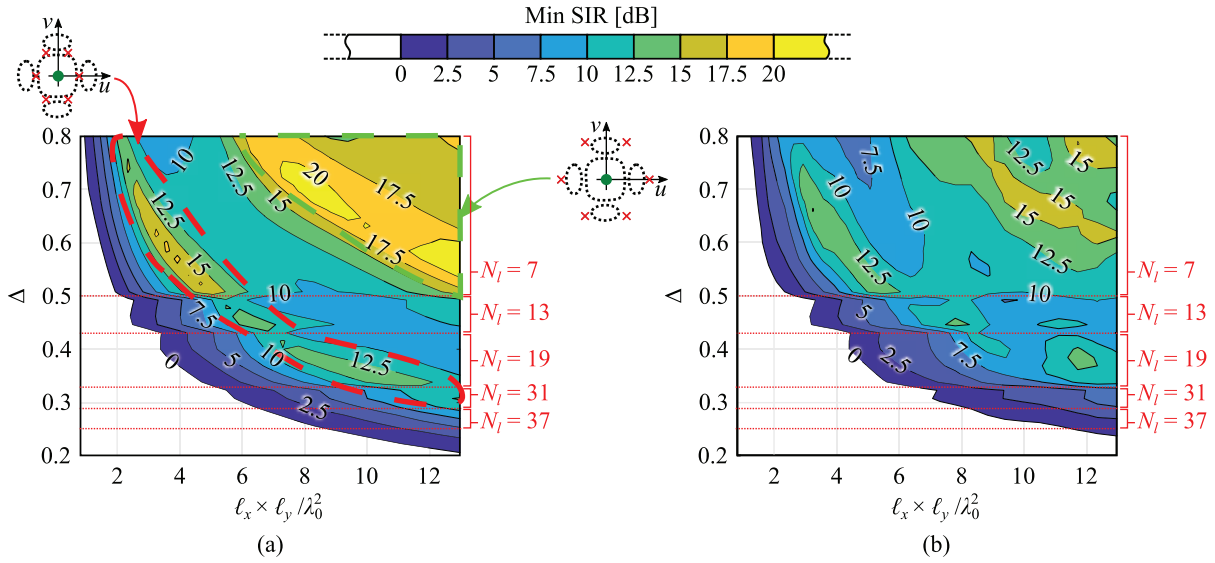


Fig. 8. Contour map of the minimum SIR calculated versus the electrical area and the beam separation for (a) ideal antenna and (b) connected array.

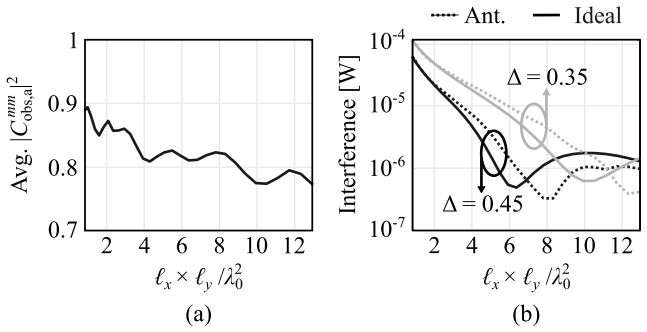


Fig. 9. (a) Array efficiency calculated as the average $\left|C^{mm}_{\text{obs,a}}\right|^2$ and (b) comparison between the average interference of the ideal and real antenna calculated for $\Delta = 0.45$, i.e., 13 beams, and $\Delta = 0.35$, i.e., 19 beams, when the electric field amplitude is $|E_0| = 1$ V/m.

map to the right since the physical area ($135 \times 135\,\text{mm}^2$) is reduced by the aperture efficiency. Moreover, the lower aperture efficiency causes a shift in the null of the patterns for a given frequency. This is highlighted in Fig. 9(b), which shows the average interference, i.e., the denominator of (17), for the real and ideal antenna, for $\Delta = 0.45$, i.e., 13 beams, and $\Delta = 0.35$, i.e., 19 beams, when $|E_0| = 1$ V/m. A shift of the minima of the interference to larger electrical sizes is observed for the real antenna, which explains the reduction of the SIR in Fig. 8(b) with respect to Fig. 8(a).

The study of the SIR assumed an equidistant sampling in the *uv*-space. An equidistant sampling in the angular space, i.e., $\theta\phi$-space, would lead to a lower SIR performance, due to the denser arrangement of directions closer to $\theta = 0$ and consequently a higher interference.

## IV. Conclusion

The observable field concept has been extended to planar geometries to characterize the multibeam performance of arrays for wireless communications. Analytical expressions for the radiation from square and circular domains have been used for efficient calculation of the observable far-field patterns.

These concepts have been used to assess the SIR of a wideband connected array prototype and to relate the maximum number of beams to the frequency and the electrical size of the antenna. The observable field represents the benchmark for a given antenna size in terms of maximum directivity. The presented approach allows to compare a given antenna design to the benchmark and to identify an upper bound for the maximum number of orthogonal beams that can be realized by the antenna.

## References

[1] E. G. Larsson, O. Edfors, F. Tufvesson, and T. L. Marzetta, "Massive MIMO for next generation wireless systems," *IEEE Commun. Mag.*, vol. 52, no. 2, pp. 186–195, Feb. 2014.

[2] W. Hong et al., "Multibeam antenna technologies for 5G wireless communications," *IEEE Trans. Antennas Propag.*, vol. 65, no. 12, pp. 6231–6249, Dec. 2017.

[3] *NR; Base Station (BS) Radio Transmission and Reception*, document 38.104, 3GPP, Valbonne, France, Dec. 2024. [Online]. Available: https://www.3gpp.org/ftp/Specs/archive/38_series/38.104/

[4] D.-M. Sun, Z.-C. Hao, W.-Y. Liu, and C.-Y. Ding, "An ultrawideband dual-polarized phased array antenna for sub-3–GHz 5G applications with a high polarization isolation," *IEEE Trans. Antennas Propag.*, vol. 71, no. 5, pp. 4055–4065, May 2023.

[5] M. H. Novak, F. A. Miranda, and J. L. Volakis, "Ultra-wideband phased array for millimeter-wave ISM and 5G bands, realized in PCB," *IEEE Trans. Antennas Propag.*, vol. 66, no. 12, pp. 6930–6938, Dec. 2018.

[6] S. M. Moghaddam, J. Yang, and A. U. Zaman, "Fully-planar ultra-wideband tightly-coupled array (FPU-TCA) with integrated feed for wide-scanning millimeter-wave applications," *IEEE Trans. Antennas Propag.*, vol. 68, no. 9, pp. 6591–6601, Sep. 2020.

[7] T.-L. Zhang, L. Chen, S. M. Moghaddam, A. U. Zaman, and J. Yang, "Millimeter-wave ultrawideband circularly polarized planar array antenna using bold-C spiral elements with concept of tightly coupled array," *IEEE Trans. Antennas Propag.*, vol. 69, no. 4, pp. 2013–2022, Apr. 2021.

[8] R. Ozzola, A. Neto, U. Imberg, and D. Cavallo, "Connected slot array with interchangeable ADL radome for sub-8 GHz 5G applications," *IEEE Trans. Antennas Propag.*, vol. 72, no. 1, pp. 992–997, Jan. 2024.

[9] I. Tzanidis et al., "*Method and apparatus for miniaturization of MIMO systems via tightly coupled antenna array*," U.S. Patent 0 334 565 A1, Nov. 13, 2014.

[10] R. Ozzola, D. Cavallo, and A. Neto, "On the relation between beam coupling and feed coupling in wideband antenna arrays," *IEEE Trans. Antennas Propag.*, vol. 70, no. 1, pp. 260–267, Jan. 2022.

[11] M. Akrout, V. Shyianov, F. Bellili, A. Mezghani, and R. W. Heath Jr., "Super-wideband massive MIMO," *IEEE J. Sel. Areas Commun.*, vol. 41, no. 8, pp. 2414–2430, Aug. 2023.

[12] A. A. D'Amico and L. Sanguinetti, "Holographic MIMO communications: What is the benefit of closely spaced antennas?," *IEEE Trans. Wireless Commun.*, vol. 23, no. 10, pp. 13826–13840, Oct. 2024.

[13] A. Neto and J. J. Lee, "'Infinite bandwidth' long slot array antenna," *IEEE Antennas Wireless Propag. Lett.*, vol. 4, pp. 75–78, 2005.

[14] D. Cavallo, W. H. Syed, and A. Neto, "Connected-slot array with artificial dielectrics: A 6 to 15 GHz dual-pol wide-scan prototype," *IEEE Trans. Antennas Propag.*, vol. 66, no. 6, pp. 3201–3206, Jun. 2018.
[15] O. M. Bucci and G. Franceschetti, "On the degrees of freedom of scattered fields," *IEEE Trans. Antennas Propag.*, vol. 37, no. 7, pp. 918–926, Jul. 1989.
[16] A. D. Yaghjian and S. R. Best, "Impedance, bandwidth, and Q of antennas," *IEEE Trans. Antennas Propag.*, vol. 53, no. 4, pp. 1298–1324, Apr. 2005.
[17] M. Gustafsson, C. Sohl, and G. Kristensson, "Physical limitations on antennas of arbitrary shape," *Proc. Roy. Soc. A, Math., Phys. Eng. Sci.*, vol. 463, no. 2086, pp. 2589–2607, Oct. 2007.
[18] P.-S. Kildal, E. Martini, and S. Maci, "Degrees of freedom and maximum directivity of antennas: A bound on maximum directivity of non-superreactive antennas," *IEEE Antennas Propag. Mag.*, vol. 59, no. 4, pp. 16–25, Aug. 2017.
[19] B. Biscontini, A. Murillo, J. Segador, and I. González, "Active antenna architectures for enhanced 5G system performance," in *Proc. Eur. Conf. Antennas Propag.*, Mar. 2020, pp. 1–5.
[20] C. Ehrenborg and M. Gustafsson, "Fundamental bounds on MIMO antennas," *IEEE Antennas Wireless Propag. Lett.*, vol. 17, pp. 21–24, 2018.
[21] C. Ehrenborg and M. Gustafsson, "Physical bounds and radiation modes for MIMO antennas," *IEEE Trans. Antennas Propag.*, vol. 68, no. 6, pp. 4302–4311, Jun. 2020.
[22] C. Ehrenborg, M. Gustafsson, and M. Capek, "Capacity bounds and degrees of freedom for MIMO antennas constrained by Q-factor," *IEEE Trans. Antennas Propag.*, vol. 69, no. 9, pp. 5388–5400, Sep. 2021.
[23] S. Mikki, "The Shannon information capacity of an arbitrary radiating surface: An electromagnetic approach," *IEEE Trans. Antennas Propag.*, vol. 71, no. 3, pp. 2556–2570, Mar. 2023.
[24] L. Passalacqua, C. Yepes, E. Martini, and S. Maci, "Q-bounded maximum directivity of self-resonant antennas," *IEEE Trans. Antennas Propag.*, vol. 71, no. 12, pp. 9549–9558, Dec. 2023.
[25] L. Passalacqua, C. Yepes, A. M. Barrera, B. Biscontini, E. Martini, and S. Maci, "Maximum gain of lossy antennas without and with Q-bounds," *IEEE Trans. Antennas Propag.*, vol. 72, no. 4, pp. 3033–3043, Apr. 2024.
[26] A. Debard, A. Clemente, A. Tornese, and C. Delaveaud, "On the maximum end-fire directivity of compact antenna arrays based on electrical dipoles and Huygens sources," *IEEE Trans. Antennas Propag.*, vol. 71, no. 1, pp. 299–308, Jan. 2023.
[27] M. Gustafsson, "Shadow area and degrees of freedom for free-space communication," *IEEE J. Sel. Areas Inf. Theory*, doi: 10.1109/JSAIT.2025.3600363.
[28] F. Puggelli, B. Biscontini, E. Martini, and S. Maci, "Maximizing independent channels and efficiency in BTS array antennas via EM degrees of freedom," *IEEE Trans. Antennas Propag.*, vol. 73, no. 6, pp. 3444–3458, Jun. 2025.
[29] A. Neto, N. Llombart, and A. Freni, "The observable field for antennas in reception," *IEEE Trans. Antennas Propag.*, vol. 66, no. 4, pp. 1736–1746, Apr. 2018.
[30] A. Neto, A. F. Bernardis, D. Emer, A. Freni, and N. Llombart, "The observable field in complex scattering scenarios," *IEEE Trans. Antennas Propag.*, vol. 68, no. 7, pp. 5544–5555, Jul. 2020.
[31] R. G. Tapia Barroso, "Study on the number of independent beams from planar domains," M.S. thesis, Dept. Electrical Engineering, Mathematics and Computer Science, Delft University of Technology, Delft, The Netherlands, 2023.
[32] A. Mazzinghi et al., "Large depth of field pseudo-Bessel beam generation with a RLSA antenna," *IEEE Trans. Antennas Propag.*, vol. 62, no. 8, pp. 3911–3919, Aug. 2014.
[33] G. Minatti et al., "Modulated metasurface antennas for space: Synthesis, analysis and realizations," *IEEE Trans. Antennas Propag.*, vol. 63, no. 4, pp. 1288–1300, Apr. 2015.
[34] A. Pascual Laguna, D. Cavallo, J. J. A. Baselmans, and N. Llombart, "Focused connected array antenna as a broadband beam-steering feed for quasi-optical system," *IEEE Trans. Antennas Propag.*, vol. 70, no. 7, pp. 5995–6000, Jul. 2022.
[35] R. Ozzola, D. Cavallo, A. Freni, N. Llombart, and A. Neto, "A benchmark for the number of independent line of sight links on a given volume platform," *IEEE Trans. Antennas Propag.*, vol. 70, no. 12, pp. 12071–12080, Dec. 2022.
[36] S. Stein, "On cross coupling in multiple-beam antennas," *IRE Trans. Antennas Propag.*, vol. 10, no. 5, pp. 548–557, Sep. 1962.
[37] E. Darve, "The fast multipole method: Numerical implementation," *J. Comput. Phys.*, vol. 160, no. 1, pp. 195–240, May 2000.
[38] A. Mazzinghi and A. Freni, "Analytical evaluation of the power radiated by sources arbitrarily distributed on a surface," *IEEE Trans. Antennas Propag.*, vol. 70, no. 12, pp. 12376–12380, Dec. 2022.
[39] T. G. Vasiliadis, A. G. Dimitriou, and G. D. Sergiadis, "A novel technique for the approximation of 3-D antenna radiation patterns," *IEEE Trans. Antennas Propag.*, vol. 53, no. 7, pp. 2212–2219, Jul. 2005.